Human-induced intensification of terrestrial water cycle in dry regions of the globe

Check for updates

Yansong Guan [1], Xihui Gu [1,2,3,4,5,6,7] ✉, Louise J. Slater [8], Xueying Li [9], Jianfeng Li [10], Lunche Wang [11,12], Xiongpeng Tang [13,14], Dongdong Kong[1,7] & Xiang Zhang[15] ✉

Anthropogenic climate change (ACC) strengthens the global terrestrial water cycle (TWC) through increases in annual total precipitation (PRCPTOT) over global land. While the increase in the average global terrestrial PRCPTOT has been attributed to ACC, it is unclear whether this is equally true in dry and wet regions, given the difference in PRCPTOT changes between the two climatic regions. Here, we show the increase in PRCPTOT in dry regions is twice as fast as in wet regions of the globe during 1961–2018 in both observations and simulations. This faster increase is projected to grow with future warming, with an intensified human-induced TWC in the driest regions of the globe. We show this phenomenon can be explained by the faster warming and precipitation response rates as well as the stronger moisture transport in dry regions under ACC. Quantitative detection and attribution results show that the global increase in PRCPTOT can no longer be attributed to ACC if dry regions are excluded. From 1961–2018, the observed PRCPTOT increased by 5.63%~7.39% (2.44%~2.80%) over dry (wet) regions, and as much as 89% (as little as 5%) can be attributed to ACC. The faster ACC-induced TWC in dry regions is likely to have both beneficial and detrimental effects on dry regions of the globe, simultaneously alleviating water scarcity while increasing the risk of major flooding.

The terrestrial water cycle (TWC) is an essential component of the climate system[1], and directly impacts water resources, agriculture, and ecosystems worldwide[2–5]. Global warming has contributed to strengthening TWC[6–8], as reflected in the increase in global annual total precipitation (PRCPTOT)[9–11]. However, temporal trends in terrestrial PRCPTOT exhibit considerable spatial heterogeneity, with different climatic regions showing dissimilar trend directions and magnitudes[11–13]. Contrary to the well-known paradigm that dry regions are expected to become drier, and wet regions wetter, a faster and stronger increase of PRCPTOT has been found in dry regions compared to wet regions of the globe[14,15]. This increase in PRCPTOT in dry regions is generally compensated or overcompensated by warming-induced increases in evapotranspiration[7,8], so it does not always lead to increases in water availability[14], despite a growing risk of short-duration rainfall extremes[16]. Understanding the divergent responses of the TWC (e.g., PRCPTOT changes) to warming in dry and wet land regions is essential for infrastructural planning, water resource management, and sustainable development.

There is growing evidence that anthropogenic climate change (ACC) intensifies the TWC through atmospheric thermodynamic and dynamic processes[17–19]. Warming increases atmospheric humidity and modulates circulation patterns, leading to regional upward motions with moisture convergence, which further enhances PRCPTOT[7,18,20]. Faster warming in certain regions is likely to create more favorable conditions for precipitation generation[21], such as a reduction in surface pressure and increase in water vapor. It is still unclear, however, whether there are differences in warming and the rates of change in precipitation per unit warming between dry and wet regions. Different external forcings have opposite effects on warming, with greenhouse gas emissions (GHG) leading to global warming effects[22] while anthropogenic aerosol emissions (AER) lead to regional cooling effects[23,24]. Hence, the coupled response of the climate system to various external forcings[25] could explain the divergent changes in PRCPTOT in dry and wet regions in recent decades[26,27]. Given that GHG (AER) are projected to increase (decrease) in the coming decades, it remains unclear whether the different changes in PRCPTOT in dry and wet land regions might continue or even be amplified in the future.

The influence of ACC on PRCPTOT has been quantified in different regions of the globe[1,9,28,29]. For instance, it is very likely (probability > 90%) that ACC explains the observed increase in terrestrial PRCPTOT over the

Northern Hemisphere during 1952–2011[1]. However, considering the much greater increase in PRCPTOT over dry regions compared to wet regions, it is necessary to assess whether the ACC signal is equally detectable in both climates. In other words, is the human-induced intensification of the global TWC, as detected in previous studies, mainly contributed by the increase in PRCPTOT over dry regions? Detection and attribution analysis must be conducted to quantify the contributions of different external forcings to the observed increase in PRCPTOT in both regions.

In this study, we investigate the changes in normalized PRCPTOT over dry and wet land regions using multiple observed datasets (Supplementary Table 1). We then confirm the difference in PRCPTOT changes obtained from climate simulations conducted with different historical external forcings (Supplementary Table 2) and Shared Socio-economic Pathway (SSP) projections (Supplementary Table 3) from the Coupled Model Inter-comparison Project Phase 6 (CMIP6; Supplementary Table 4)[30]. We explain the different changes based on two aspects: the precipitation ~temperature relationship and the response of atmospheric moisture to global warming. Finally, two detection and attribution methods are employed to provide quantitative evidence for the role of ACC and its contribution to the observed changes in PRCPTOT in dry and wet regions. All acronyms are listed in Supplementary Table 5.

Results

Human-induced changes in PRCPTOT in dry and wet land regions

To demonstrate the strengthening of the TWC, the observed PRCPTOT changes during 1961–2018 are estimated using three gridded datasets (HadEX3, CRU, and GPCC; see Methods) based on widespread gauge-based stations across global land (11800–67298 stations). Data-gap information for each global terrestrial grid cell during 1961–2018 is offered by the HadEX3 dataset. A total of 1432 grid cells (2.5° × 2.5°; covering 59.2% of global terrestrial grid cells, excluding Antarctica) with missing values below 10%, are selected as the study area (Supplementary Fig. 1a). Dry (wet) regions are identified as the grid cells in which the climatological mean PRCPTOT lies within bottom (top) 30% of the 1432 grid cells[14,31]. The dry regions are primarily located in western Australia, and central and north-eastern Asia. The wet regions are discretely located in southeastern Southern America, eastern North America, western and northern Europe, south-eastern Asia, and western Africa (Supplementary Fig. 1c). These spatial patterns of dry and wet regions are basically consistent with previous studies based on different criteria (e.g., aridity index, Palmer drought severity index, and other metrics[32–35]). Furthermore, we test whether our results are sensitive to the selection of 20% and 40% as thresholds for the identification of dry and wet regions (Supplementary Fig. 1b and d).

All three observed datasets show increasing PRCPTPOT during 1961–2018 over dry and wet regions, at rates of 1.1% per decade ($p < 0.05$) and 0.2% per decade ($p = 0.18$) (Fig. 1a). The increasing rate of observed PRCPTOT is six times faster in dry regions compared to wet regions. The CMIP6 simulations under the historical all forcing scenario (ALL) also reveal increasing rates in dry (1.2% decade^{-1}) and wet (0.2% decade^{-1}) regions during 1961–2018 (Fig. 1b). The above trends in PRCPTOT over dry and wet regions were also found in previous studies[14,36]. However, the natural forcing simulations (NAT) show no significant changes in PRCPTOT in either region. In other words, the faster increase in dry regions fails to be captured if anthropogenic forcing (ANT) is removed from ALL (Fig. 1f). Under ANT, there exist significant ($p < 0.01$) increases in PRCPTOT over both dry (2.0% decade^{-1}) and wet (0.2% decade^{-1}) regions, but the difference in increasing rates between the two regions is substantially enlarged (i.e., from sixfold under ALL to tenfold under ANT; Fig. 1c). Consistent and significant increases in PRCPTOT are found in dry regions (Fig. 1d, e) under both of the main two external forcings (i.e., GHG and AER) in ANT. However, PRCPTOT exhibits a significant decrease under AER over wet regions. In the wet regions (mostly located in monsoon zones), AER inhibits the development of the monsoon and reduces atmospheric humidity through aerosol-cloud interactions[37,38]. Therefore, the combined effects of GHG and AER (i.e., approximately ANT) are responsible for the faster increase of PRCPTOT in dry regions compared to wet regions.

We evaluate the gradient change in PRCPTOT increase in dry and wet regions (Supplementary Fig. 2). During 1961–2018, both observed and simulated precipitation show the stronger signal of PRCPTOT increase when drier regions (from bottom 20%–30% grids to bottom 10% grids) are selected. In wet regions, although observed PRCPTOT increase is not associated with the selection of wetter grids, simulated PRCPTOT changes show the weaker signal of PRCPTOT increase when wetter regions (from top 20%–30% grids to top 10% grids) are selected. Therefore, there is a gradient change in dry and wet regions, i.e., a greater (smaller) magnitude of PRCPTOT increase in drier (wetter) regions.

We then examine projections of PRCPTOT in dry and wet regions under different SSPs (Supplementary Fig. 3). Under the lowest emission scenario (SSP126), projected increases in PRCPTOT are weak in both regions during 2043–2100 (the same length as the historical period 1961–2018), and this weak growth is more evident in dry regions compared to wet regions. However, significant increases in PRCPTOT are projected over both regions, as well as a faster increase in dry regions, under the middle emission scenarios (SSP245 and SSP370). As the emissions increase (SSP585), both the rates of change and the differences between the two regions increase. These projections corroborate the results seen in the historical simulations.

Despite the increase in PRCPTOT in both dry and wet regions[14,31,36], the increases in PRCPTOT in observations and simulations are faster in dry regions compared to wet regions during the historical and future periods. However, the simulations show that the faster increase in PRCPTOT in dry regions than in wet regions during the historical period emerges only when ANT is considered, and during the future period disappears under a low emission scenario, implying a faster human-induced TWC in the world's dry regions compared with wet regions. Our findings are not sensitive to the choice of threshold used to identify dry and wet regions (Supplementary Figs. 4–7).

PRCPTOT and moisture in response to warming in dry and wet regions

To understand the processes behind the strengthening of TWC in dry regions compared to wet regions under climate change, we investigate the PRCPTOT ~temperature (i.e., near-surface air temperature) relationship under different external forcings (Fig. 2a–d). During the historical period (1961–2018) under ALL, the regional warming rate was much faster in dry regions (0.33 K·decade^{-1}) compared with wet regions (0.23 K·decade^{-1}; Fig. 2a). However, if ANT is removed from ALL, this difference in warming rates almost disappears (0.004 K·decade^{-1} for dry and 0.01 K·decade^{-1} for wet under NAT). The faster warming rate in dry regions compared to wet regions under ACC results from the stronger warming effects in dry regions under GHG and the stronger cooling effects in wet regions under AER. In a warmer future (2043–2100), the higher the emissions, the greater the difference in warming rates that can be expected between dry and wet regions.

Despite the faster warming rate in dry regions, the extent to which PRCPTOT may respond to this regional warming also needs to be assessed within each of the CMIP6 models (Fig. 2b) as well in as large single-model ensembles[39] (Fig. 2c, d). We find that PRCPTOT increases in both regions with regional warming under ALL, but it increases much faster in dry regions (3.07% K^{-1}) compared to wet (0.98% K^{-1}) regions (Fig. 2b). Under NAT, the response of PRCPTOT to regional warming is weakly positive (0.71% K^{-1}) in dry regions, and is even negative (–1.30% K^{-1}) in wet regions. When considering the influence of ACC, on the one hand, we note that the faster response rate of dry regions compared to wet regions under the GHG scenario is also true under ALL. Under AER, however, wet regions also have a higher sensitivity of PRCPTOT to the cooling effects of aerosols compared with dry regions. These synergetic effects of GHG and AER lead to the faster increase of PRCPTOT per unit warming in dry regions relative to wet regions. As emissions grow in the future, we find the response of PRCPTOT
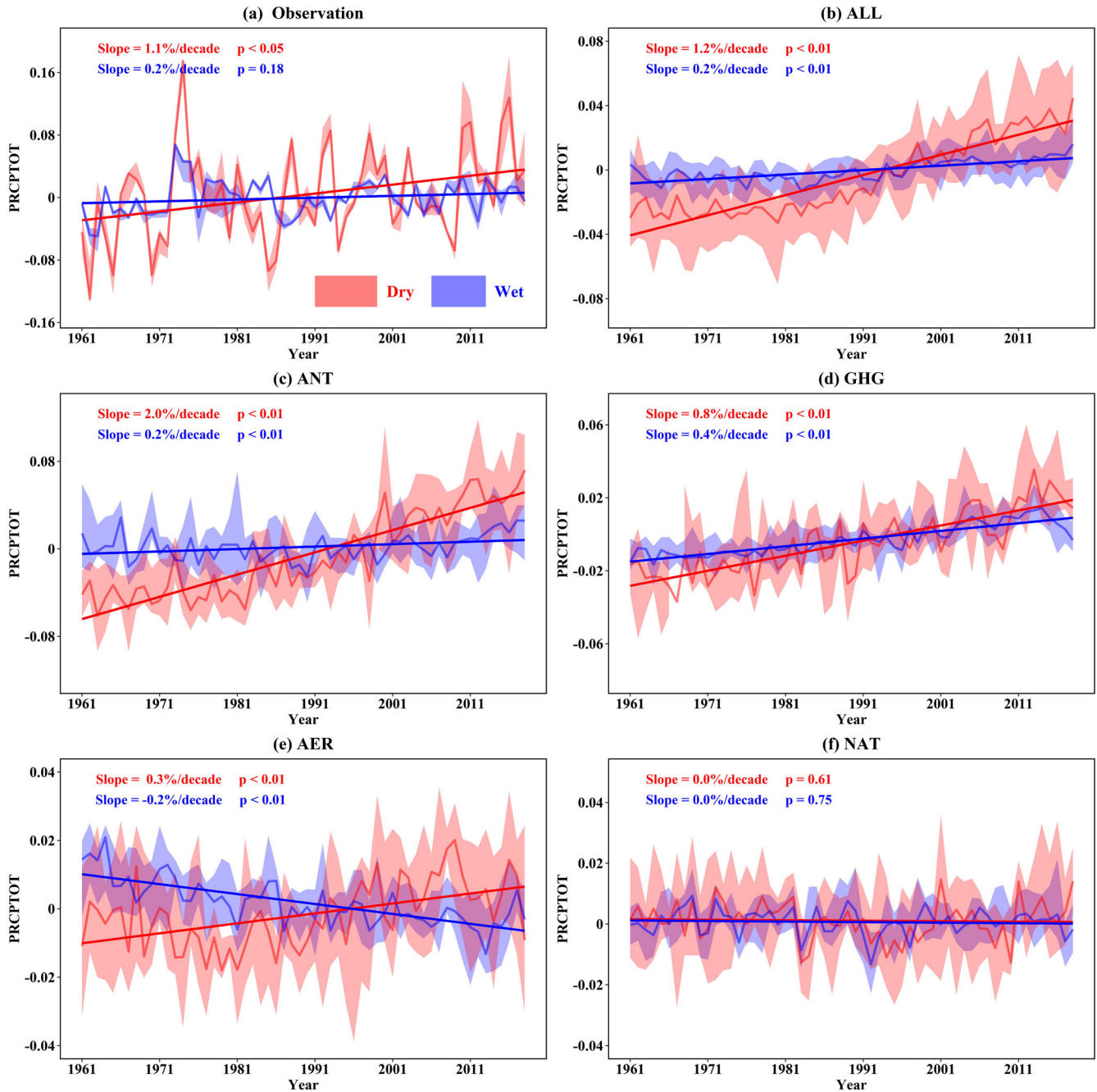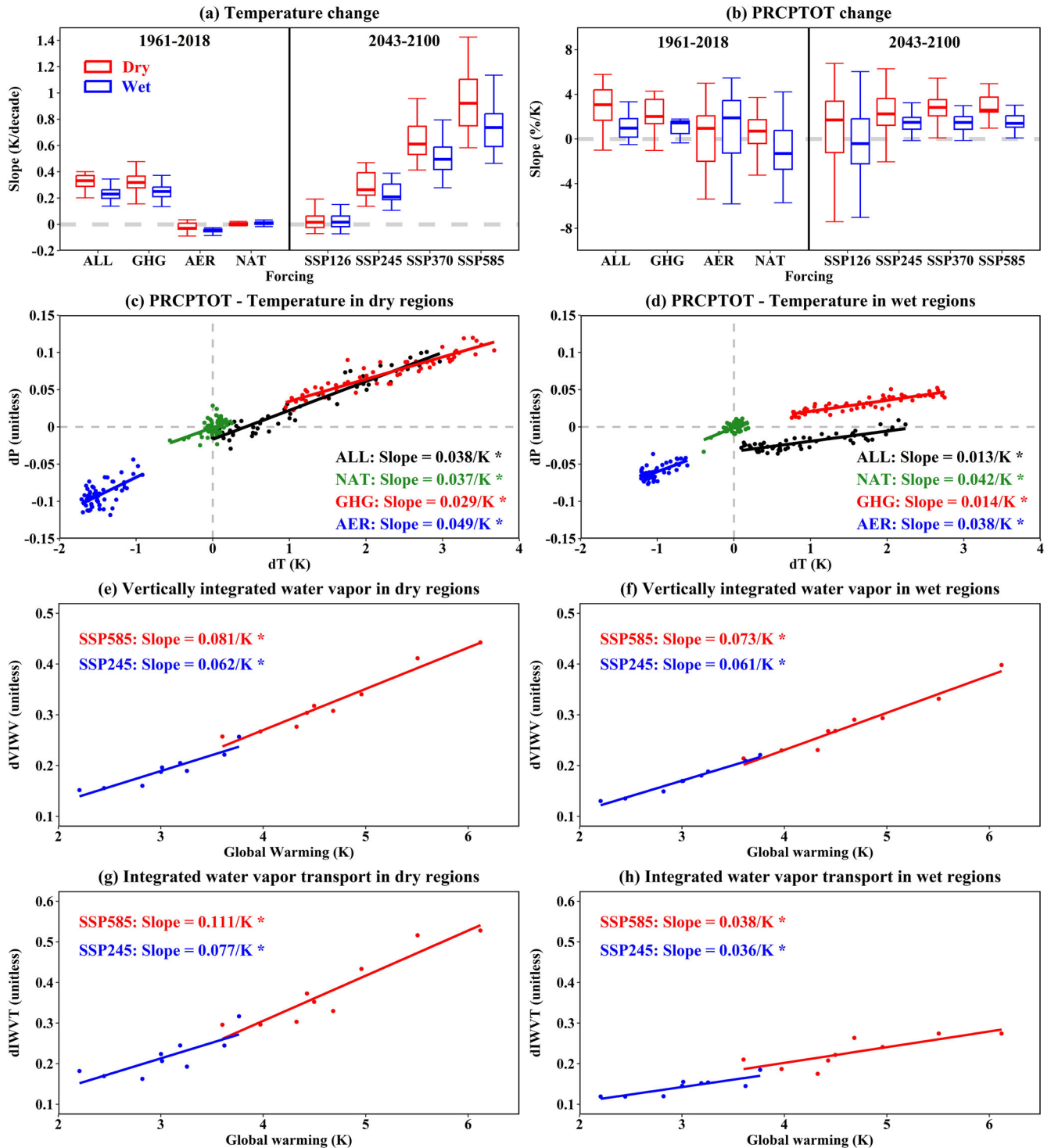
Fig. 1 | Observed and simulated changes in total precipitation (PRCPTOT) in global dry and wet regions during 1961–2018. Dry/wet regions are identified as the grid cells with PRCPTOT values in the bottom/top 30% of all PRCPTOT values across the global land surface (see Supplementary Fig. 1c). **a** Normalized PRCPTOT (unitless) in dry and wet regions in multiple observed datasets. The time series represent the median of the area-averaged PRCPTOT from the ensemble of observed datasets; the straight lines represent the linear trend; the ribbons represent the range (minimum and maximum) within these observed datasets; the slope indicates the linear trend estimated using Sen's slope; and the *p*-value indicates the trend significance estimated using the Mann-Kendall test. **b**–**f** The same as (**a**) but for CMIP6 simulations under different historical forcings (see Methods), i.e., ALL (**b**), ANT (**c**), GHG (**d**), AER (**e**), and NAT (**f**). In (**b**–**f**) the ribbons indicate the 25–75% uncertainty ranges of all individual CMIP6 models under the corresponding forcings. The figure is done in the software R 4.1.2 (https://cran.r-project.org/bin/windows/).

to warming is larger in both regions, with a smaller spread among models, but this response is more sensitive in dry regions.

To evaluate the plausibility of the difference in PRCPTOT responses to warming between dry and wet regions found in the CMIP6 models, we conduct a separate and in-depth analysis using CanESM5 experiments with 50 ensemble members under different external forcings (Fig. 2c, d). The changes in PRCPTOT (*dP*) or temperature (*dT*) in both regions are computed by taking the annual anomalies during 1961–2018 (historical period) relative to the 1861–1900 (early industrial period) mean. The changes

observed in dry and wet regions, including the regional warming rate and the PRCPTOT response rate under different external forcings, are consistent between the individual CMIP6 models and the large single-model ensemble. In both regions under GHG, *dP* and *dT* show a positive association some distance away from the coordinate origin, while under NAT, both *dP* and *dT* fluctuate around the climate state of the early industrial revolution. Our findings indicate that the positive response of PRCPTOT to warming in wet and dry regions is consistent across multiple models under ALL and GHG, but it is not robust under NAT.

Fig. 2 | PRCPTOT and water vapor changes in dry and wet regions as a function of warming. Dry/wet regions are identified as the grid cells with PRCPTOT values in the bottom/top 30% of all PRCPTOT values across the global land surface. **a** Boxplots show temporal trends of regionally averaged near-surface air temperature (hereafter temperature, unit: K/decade) in dry and wet regions during 1961–2018 under different external forcings (i.e., ALL, GHG, AER, and NAT) and during 2043–2100 under different future scenarios (i.e., SSP126, SSP245, SSP370, and SSP585) based on 309 realizations of CMIP6 (see Supplementary Table 2 and 3), respectively. **b** The same as (**a**) but for temporal trends of regionally averaged PRCPTOT changes as a function of temporal trends of regionally averaged temperature changes (%/K) in dry and wet regions, respectively. In **a**, **b**, the statistics in the box plots from the upper to lower bound represent the value of Q3 + 1.5 (Q3–Q1), third quartile (Q3), median (horizontal line), first quartile (Q1), and Q1–1.5 × (Q3–Q1) successively. **c**, **d** PRCPTOT-temperature relations

($\Delta P \sim \Delta T$, unit: K^{-1}) in dry (**c**) and wet (**d**) regions estimated by the CanESM5 experiments with 50 ensemble members. In **c**, **d** the dots indicate the regionally averaged annual anomalies (temperature or precipitation) during 1961–2018 relative to the 1861–1900 mean for the ensemble mean under different external forcings. **e**–**h** Regionally averaged normalized vertically integrated water vapor (VIWV; **e**, **f**) and integrated water vapor transport (IWVT; **g**, **h**) changes in dry (**e**, **g**) and wet (**f**, **h**) regions as a function of global warming (K^{-1}), respectively. In **e**–**h**, blue (red) dots represent the differences of values between the 2070–2099 mean under SSP245 (SSP585) and the 1961–1990 mean under ALL for the individual CMIP6 models, using the first ensemble member (i.e., r1i1p1f1) for each model. In **c**–**h** the solid lines represent the best-fit linear regression through all points of a scenario; the slope and the p-value as in Fig. 1; the symbol "*" shows the slope is significant at the 0.01 level. The figure is done in the software R 4.1.2 (https://cran. r-project.org/bin/windows/).

We also explore the relationship between moisture and global warming in dry and wet regions using multiple models under the ALL simulation (1961–1990) and SSP245/SSP585 (2070–2099; Fig. 2e–h). Both moisture content (vertically integrated water vapor; see Methods) and moisture transport (vertically integrated water vapor transport) show a linear positive association with global warming in dry and wet regions. Under SSP245/SSP585, moisture content is projected to increase by 6.2%/8.1% per unit of global warming in dry regions, and these percentages are very similar with those in wet regions (6.1%/7.3%). However, the moisture transport is projected to be much stronger in dry regions (7.7%/11.1% per unit warming) than in wet regions (3.6%/3.8% per unit warming).

Overall, human-induced warming occurs faster in dry regions compared to wet regions, and the magnitude of the increase in PRCPTOT is also much larger in dry regions. Both faster warming and precipitation response rates lead to a greater PRCPTOT increase in dry regions than in wet regions[40], which can be explained by the warming-related increases in moisture content and transport in both regions, and especially the stronger increases of moisture transport in dry regions. The relationships between PRCPTOT/moisture and warming are not sensitive to the division into dry and wet regions (Supplementary Figs. 8–9).

Detection and attribution of PRCPTOT changes in dry and wet land regions

It has been widely reported that the effect of ACC is detectable in the increase in global TWC[1,31,41]. However, given the much faster increase in PRCPTOT in dry regions than in wet regions, we hypothesize that the signal of global ACC may be absent if dry regions are excluded from the world's land surface. To test this hypothesis, we employ two detection and attribution methods to identify the anthropogenic fingerprint from observed increases in PRCPTOT over dry and wet regions during 1961–2018.

Using a pattern-based detection and attribution method[42–44] (see Methods), we employ a rotated empirical orthogonal function (REOF)[45–47] to extract the leading EOF (as a fingerprint) and the corresponding temporal principal component (PC) from PRCPTOT under ALL and SSP585 during 1901–2100 (Supplementary Figs. 10–12). The leading modes (EOF1 and PC1) explain between 84.6%–92.7% of the total variance of PRCPTOT in dry, wet, and dry+wet regions, suggesting that they capture most of the original PRCPTOT signal. The changes in PC1 are highly consistent with the long-term changes in global mean temperature, indicating that the fingerprint is a signal of global warming. These positive responses to global warming are found in ~90% of dry regions and ~70% of wet regions in the spatial patterns (EOF1).

We then project observed and simulated PRCPTOT onto the model-based fingerprints in dry and wet regions to quantify the ACC signal and its significance (Fig. 3 and Supplementary Figs. 13–14). During the period 1961–2018, observations in dry+wet regions exhibit an increasing resemblance to the fingerprint, as illustrated by the positive trend ($p < 0.01$) of fingerprint projections (Fig. 3e). The signal-to-noise ratio (SNR) analysis reveals that the ACC signal during 1961–2018 is detectable with 90% confidence in dry+wet regions (SNR = 1.73; Fig. 3f), consistent with previous studies[1,41,42]. In comparison with dry+wet regions, a consistent increasing resemblance to the fingerprint can be seen in dry regions where the ACC signal is also detectable (SNR = 1.68; Fig. 3a, b). Despite the presence of a positive trend in the fingerprint projections, the ACC signal fails to be detected in wet regions (SNR = 1.31; Fig. 3c, d).

We also estimate the time of emergence based on simulated SNR under the ALL simulation and SSP585 scenario during 1911–2100, testing the robustness of the ACC signal in dry regions (Supplementary Fig. 15). Both dry and wet regions show increasing trends in the SNR under SSP585, but a faster increase in SNR is found in dry regions (Supplementary Fig. 15a, c, and e). The ACC signal becomes significantly detectable in simulated PRCPTOT in dry regions in ~2012 and ~2021 at the 90% and 99% confidence levels, respectively, supporting the presence of a detectable ACC signal in PRCPTOT observations (Fig. 3a, b). In wet regions, however, an ACC signal only becomes

detectable by the years ~2021 and ~2032. In both regions, the reduction in noise amplitude with longer trend-fitting periods (Supplementary Fig. 15b, d, and f) is the main cause of the increase in the SNR[48,49]. Nevertheless, the noise amplitude and SNR are larger in dry regions than in wet regions, suggesting that the historical ACC signal is more pronounced in dry regions.

Finally, we employ the optimal fingerprint method[50,51] (see Methods) to validate the detection and attribution results from the REOF-based method, and more importantly to quantify contributions of external forcings to observed changes in PRCPTOT during 1961–2018 (Fig. 4 and Supplementary Figs. 16–17). In the optimal fingerprint method, observed PRCPTOT is regressed against historical simulations under one forcing (one-signal analyses) or two forcings (two-signal analyses), and the scaling factor (estimated by ordinary least squares (OLS) or total least squares (TLS)) is used to scale simulated PRCPTOT such that it matches the observed changes in PRCPTOT. In dry regions, both the OLS- and TLS-estimated scaling factors of simulated PRCPTOT are significantly above zero under the ALL, ANT, and GHG simulations based on the one-signal analyses; however, this is not the case under the NAT or AER simulations (Fig. 4a, d). In wet regions, there is no scaling factor significantly greater than zero. The one-signal analysis results are also supported by two-signal analyses, which also show that the PRCPTOT responses for the ALL, ANT, and GHG simulations are distinct from those under NAT in dry regions but not in wet regions (Fig. 4b, e). It can thus be concluded from the scaling factor analyses that the simulated responses are detectable (indetectable) in observed PRCPTOT in dry (wet) regions only if (regardless of whether) ACC is considered in the model simulations. This finding is consistent with the REOF-based assessment, and thus strengthens the evidence that ACC is responsible for the faster TWC in dry regions compared to wet regions.

To further estimate the contributions of external forcings to observed changes in PRCPTOT, the linear trends in simulated PRCPTOT under each external forcing are multiplied by the corresponding scaling factors obtained from the one-signal analyses (Fig. 4c, f). From 1961–2018, observed PRCPTOT has increased by 5.63%~7.39% (2.44%~2.80%) in dry (wet) regions based on thresholds of 20–40% to identify the dry/wet regions. The increases in PRCPTOT in dry (wet) regions attributed to ALL, ANT, and GHG are 5.22%~5.82% (0.06%~1.67%), 5.02%~6.17% (−0.46%~0.21%), and 5.68%~8.20% (0.19%~1.18%), respectively, based on the OLS estimation. The proportions estimated from TLS are 6.25%~7.04% (0.94%~2.08%), 5.89%~7.07% (−0.56%~0.91%), and 6.96%~9.93% (1.18%~2.14%), respectively. In other words, the increases in PRCPTOT that are detected in the ALL simulations are comparable to the observed increases found in dry regions, but exceed the changes found in wet regions. These findings support the robustness of our attribution results in dry regions. Conversely, the lack of a robust signal of external forcings in the observed PRCPTOT in wet regions indicates larger uncertainties. Our detection and attribution results are not sensitive to the choice of threshold used to identify dry and wet regions (Supplementary Figs. 11–17).

Discussion

In this study, we find an intensified TWC (i.e., faster PTCPTOT increase) in dry regions than in wet regions, which can be attributed to ACC. In other words, there exists a faster rate of warming and a greater increase in PRCPTOT per unit warming under the influence of ACC (mainly GHG; Figs. 2 and 4) in dry regions than in wet regions. Generally, with warming-induced atmospheric thermodynamic effects, the accumulation of surface and atmospheric energy[52] increases evapotranspiration and moisture content in both dry and wet regions[7,20]. Our study finds no significant difference in the rates of increase in moisture content per unit warming between dry and wet regions, indicating that thermodynamic effects might not be the main reason for the differences in increasing PRCPTOT rates over the two climatic regions under ACC.

The difference in the intensification of the TWC between dry and wet regions is, however, seen in the moisture transport, i.e., through warming-induced atmospheric dynamic effects. Previous studies have found that
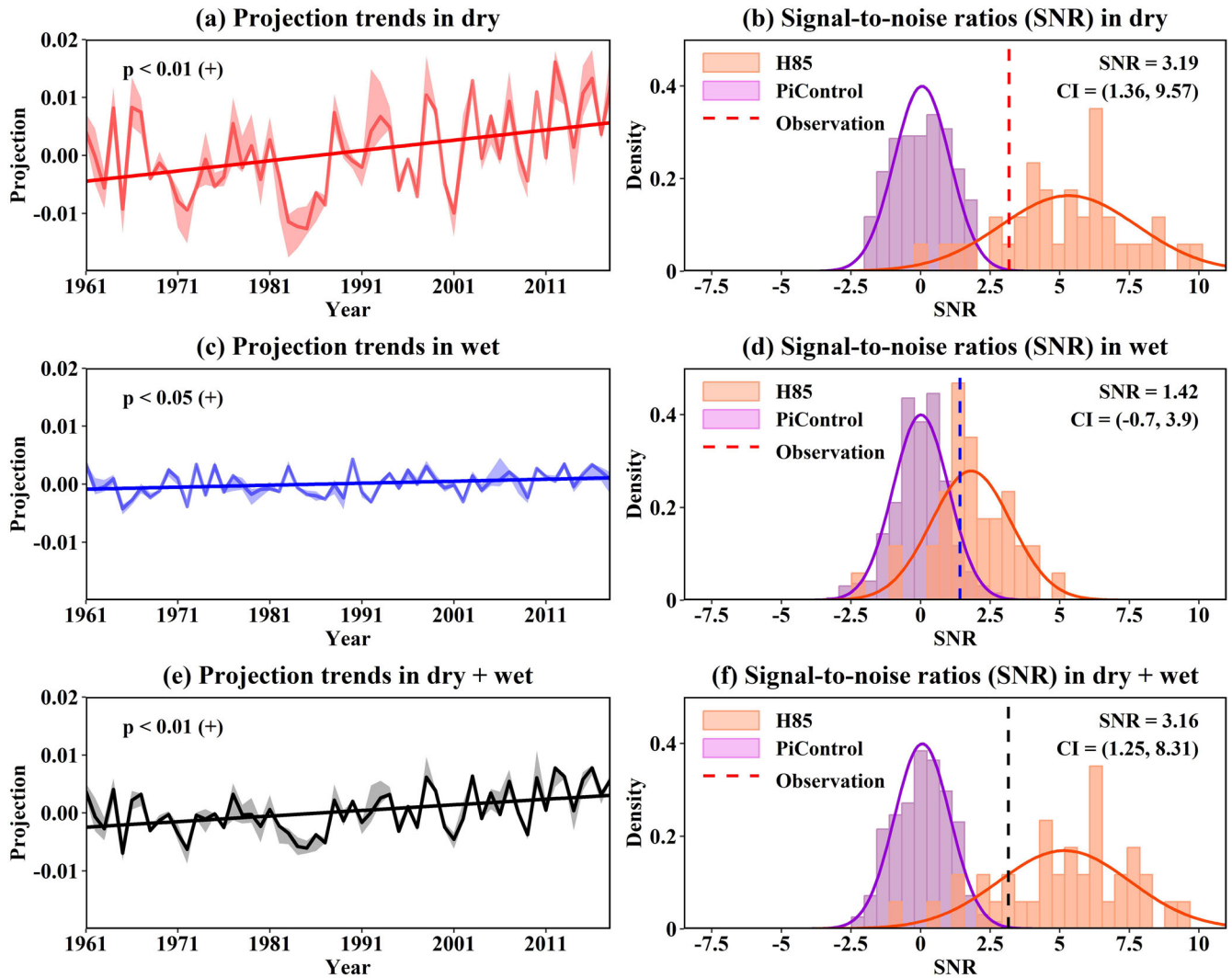
Fig. 3 | PRCPTOT in dry and wet regions from projecting observations and simulations onto the fingerprint. The dry/wet grid regions are identified from the grid cells with PRCPTOT values in the bottom/top 30% of all values across the global land surface. **a**, **c**, and **e** Projections of observed PRCPTOT in dry (**a**) wet (**c**) and dry +wet (**e**) regions during 1961–2018 onto the fingerprint. The "+" symbol indicates an upward trend; line terminology, shadow, slope, and *p*-value as in Fig. 1. **b**, **d**, and **f** Signal-to-noise ratios (SNRs) for 1961–2018 trends from observations (dashed vertical lines), PiControl simulations (purple histograms), and H85 simulations (ALL + SSP585, see Methods; orange histograms) in dry (**b**), wet (**d**) and dry+wet (**f**) regions. In (**b**) (**d**) and (**f**) the symbol "SNR" indicates the SNR value in the observations and "CI" indicates 5–95% confidence intervals (CIs) for SNR in H85 simulations; the solid curves indicate the best-fit Gaussian distribution. The figure is done in the software R 4.1.2 (https://cran.r-project.org/bin/windows/).

atmospheric circulation plays an important role in the transport of moisture to dry regions, both from adjacent oceans[53–55] and from remote oceans via teleconnection patterns[56–58]. The faster warming in dry regions amplifies dynamic processes, for example, the stronger land-ocean contrast between dry regions and adjacent oceans[59,60] strengthens the landward pressure gradient and enhances moisture transport from oceans to dry regions[54,61]. The faster warming generates an anomalous meridional temperature gradient between dry regions and other contiguous regions[26,52]. This uneven warming pattern also alters regional circulation patterns (such as jet streams and storm tracks[62,63]) over dry regions, e.g., the African easterly jet, which is displaced poleward[64] and the Asian subtropical jet, which is displaced southward[65]. These shifting circulation patterns intensify the long-distance transport of westerlies, carrying greater moisture to dry regions[66], and supporting the vorticity advection and upward motion for precipitation generation over dry regions[52].

To interpret the increase in moisture transport over dry regions under global warming, recent studies have also emphasized the importance of land–atmosphere feedbacks[61,67]. Under ACC, the faster decrease in soil moisture in dry regions[68] enhances turbulent energy transfer from the

surface to the atmosphere[69]. This stronger energy exchange increases atmospheric temperature and latent heat, amplifying the atmospheric water-holding capacity and moisture content over dry regions[70]. The faster atmospheric heat accumulation leads to low-level vertical ascent and moisture convergence, favoring the generation of precipitation in dry regions[67]. In addition, the faster decline in soil moisture also enhances the land-ocean contrast in dry regions, enhancing moisture transport[59,60]. Hence, the TWC is enhanced in dry regions by the combination of ACC-induced thermodynamic and dynamic effects, and the dynamic effects are further amplified by land–atmosphere feedbacks.

In contrast, wet regions mainly located at monsoon regions (Supplementary Fig. 1b–d) where the increase in precipitation is inhibited by warming-induced dynamic effects[71–74]. Monsoon circulation patterns tend to be controlled by atmospheric convective overturning[75], the intensity and structure of which affects moisture transport and precipitation generation. Under GHG-induced warming, the zonal sea surface temperature gradient is weakened across the equatorial Indo-Pacific[76] and the lower troposphere stratification is enhanced[77], both of which tend to reduce the strength of atmospheric overturning circulation[78]. The reduction occurs preferentially
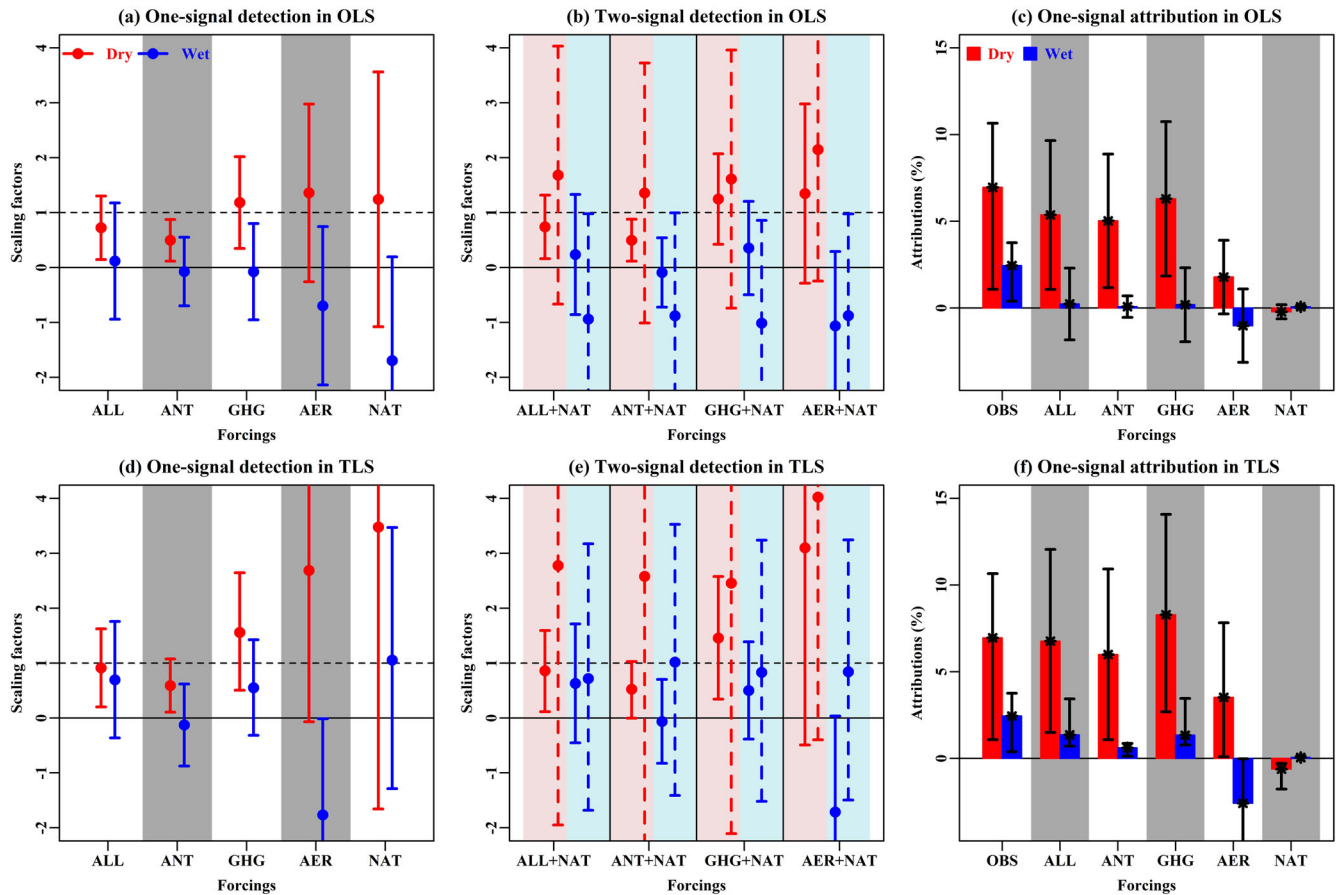
Fig. 4 | Scaling factors and attributable PRCPTOT changes in dry and wet land regions during 1961–2018. Dry/wet regions are the grid cells with PRCPTOT in the bottom/top 30% of all cells across the global land surface. **a** Optimized scaling factors based on the one-signal analysis (dots) and their 5–95% CIs (vertical lines) for PRCPTOT trends in dry and wet regions for ALL, ANT, GHG, AER, and NAT based on the one-signal analysis. **b** The same as (**a**) but based on the two-signal analysis by combining individual forcings (i.e., ALL, ANT, GHG, and AER; solid lines) and NAT (dashed lines). **c** Observed PRCPTOT changes in dry and wet regions, and attributable changes to ALL, ANT, GHG, AER, and NAT from the one-signal analysis. In (**c**) the error bars indicate the corresponding 5–95% CIs. **d–f** The same as **a–c** but with the TLS method. The figure is done in the software R 4.1.2 (https://cran.r-project.org/bin/windows/).

in the zonally asymmetric component of the tropical circulation (i.e., Walker Cell). A weakened Walker circulation could decrease the sea level pressure gradient, inhibiting moisture transport to wet (monsoon) regions[79]. In addition, under GHG-induced warming, the Hadley Cell (another component of tropical circulation) is weakened and its downward branch is expected to move toward the poles[77,80,81], weakening moisture transport to wet regions[82,83]. Therefore, although the TWC is enhanced in wet regions under GHG-induced warming by thermodynamic effects, these are partly offset by dynamic effects such as weakened tropical circulation.

Under AER, PRCPTOT in dry/wet regions shows an increasing/decreasing trend (Fig. 1e). Previous studies show the radiative cooling resulting from AER generates circumglobally stationary Rossby waves in the mid-latitudes[84], which shift the westerly jet stream (e.g., the Asian subtropical jet) southward[85]. This shift favors moisture supply from low-latitudes and moisture convergence over dry regions, resulting in precipitation generation over dry regions[52,86]. The reduction in PRCPTOT in wet regions results from reduced vertical moisture advection in response to AER over global monsoon regions. Both the AER-induced thermodynamic (reduction in atmospheric humidity) and dynamic (weakening land-ocean contrast between monsoon regions and adjacent oceans) effects cause a reduction in the vertical moisture advection over wet regions, where the thermodynamic effect is dominant[27]. Hence, without considering the effects of GHG, TWC in dry (wet) regions is enhanced (inhibited) by AER-induced atmospheric dynamic effect (thermodynamic and dynamic effects).

In the global TWC, other hydro-meteorological fluxes and stores besides precipitation (e.g., evapotranspiration (ET), runoff, soil moisture, and snow) are also involved[87]. ET acts as an important component in global TWC[88,89], due to the net difference between water supply from precipitation and water demand from ET, which can almost represent the changes in terrestrial TWC[90]. We calculate the PME (precipitation from the HadEX3 dataset minus ET from the GLEAM dataset; see Methods) to invalidate whether PRCPTOT can represent the long-term spatial patterns of aridity and humidity over land. Consistent with the PRCPTOT-based division method, PME-based dry (wet) regions are identified as the grid cells in which the climatological (1981–2010) mean PME lies within bottom (top) 30% of the 1432 grid cells. Our results represent that PME-based global dry and wet regions show consistent spatial patterns compared to PRCPTOT-based dry and wet regions, including North Russia and India (Supplementary Figs. 1 and 18). Over the PME-based dry regions, the observed and simulated PRCPTOT have the same significant increasing trends (OBS and ALL: 1.1%/decade) during 1961–2018 as PRCPTOT (OBS: 1.1%/decade; ALL: 1.2%/decade) over the PRCPTOT-based dry regions (Fig. 1 and Supplementary Fig. 19). Increasing trends of observed and simulated PRCPTOT in wet regions for two criteria are both 1/6 times of the trends of PRCPTOT in dry regions. Furthermore, PRCPTOT trends in based-PME dry and wet regions are not sensitive to the choice of threshold used to identify dry and wet regions (Supplementary Figs. 20 and 21). Therefore, if ET, the outward water flux in TWC, is not considered, the bias from the global trend of aridity and humidity over land remains negligible, implying

that our results on changes of PRCPTOT in dry and wet regions are not affected whether ET is considered for dividing dry and wet regions or not.

In addition, although previous studies have found an ACC-induced intensification in some of these processes[91–94], they can be significantly altered by anthropogenic activities (e.g., dams, reservoirs, impervious surfaces, domestic and industrial water demand, and irrigated agriculture[89,95–97]). Thus, it is challenging to separate the signal of ACC from that of anthropogenic activities for each of these fluxes and stores. Consistent with previous studies[1,14,98], only PRCPTOT is used as a metric of the intensifying TWC in this study. As an essential component of the TWC, PRCPTOT has direct impacts on water resources[99], agriculture[100,101], and ecosystems[102]. Our results highlight that the ACC signal previously detected in the global increase in PRCPTOT arises mainly from dry regions, implying that any global ACC signals captured in other stores of and fluxes of the TWC also need to be reassessed. The faster TWC in dry regions may have both beneficial and detrimental consequences, alleviating water scarcity or exacerbating regional flood risks[103]. Considering that dry regions include about half of the global population[33] (depending on how they are defined), the intensifying TWC is likely to require corresponding adaptation measures.

Methods
Observation-based datasets
We use three gridded observation-based precipitation products (Supplementary Table 1), namely HadEX3 from the Met Office Hadley Center, which has a spatial resolution of $1.875° \times 1.25°$ and covers 1901–2018[104], CRU from the Climatic Research Unit, with a spatial resolution of $0.5° \times 0.5°$ over 1901–2020[105], and GPCC from the Global Precipitation Climatology Centre, with a spatial resolution of $0.25° \times 0.25°$ over 1891–2019[106]. Considering the differences among these datasets[107], annual total precipitation (PRCPTOT) anomalies are normalized by dividing each the values of each product by its climatological (1981–2010) mean PRCPTOT.

In addition, we use the evapotranspiration (ET) from the state-of-the-art diagnostic remote sensing-based actual ET products—Global Land Evaporation Amsterdam Model dataset (GLEAM), with a spatial resolution of $0.25° \times 0.25°$ over 1981–2020[108]. By employing PME (precipitation minus evapotranspiration) in place of PRCPTOT to divide the dry and wet regions, we validate whether PRCPTOT can represent the long-term spatial patterns of aridity and humidity over land. The above datasets are interpolated to a $2.5° \times 2.5°$ spatial resolution by bilinear mapping[109].

CMIP6 outputs under historical and future scenarios
We use the historical simulations (1901–2020; Supplementary Table 2) and future projections (2021–2100; Supplementary Table 3) from the Coupled Model Intercomparison Project Phase 6 (CMIP6; Supplementary Table 4). The historical experiments include natural forcing (NAT), greenhouse-gas forcing (GHG), anthropogenic-aerosol forcing (AER), and historical climate forcing (ALL, including NAT and anthropogenic forcing (ANT)). ANT is calculated as ALL–NAT[110]. The CMIP6 future scenarios are the combination of the Representative Concentration Pathways (RCPs) and the Shared Socioeconomic Pathways (SSPs), including SSP126, SSP245, SSP370, and SSP585, from low to high emissions. As in previous studies[14,43], the ALL simulations were extended after the year 2014 with the SSP585 projections to generate combined time series (H85, 1901–2100). The unforced pre-industrial control (PiControl) experiments are used to estimate the internal climate variability. In total, the CMIP6 scenarios comprise 61 models with 309 realizations (all the realizations from each model), providing monthly precipitation ("pr", kg·m^{-2}·s^{-1}), near-surface air temperature ("tas", K), specific humidity ("hus", kg·kg^{-1}), surface air pressure ("ps", Pa), meridional winds ("va", m·s^{-1}), and zonal winds ("ua", m·s^{-1}). The above CMIP6 datasets are all interpolated to a $2.5° \times 2.5°$ spatial resolution for consistency, by using bilinear mapping.

Moisture content and transport
In this study, moisture content and transport are represented by the vertically integrated water vapor (VIWV) and vertically integrated water vapor transport (IWVT), respectively:

$$VIWV = \frac{1}{\rho g} \int_{p_t}^{p_s} q \, dp \tag{1}$$

$$IWVT = \frac{1}{\rho g} \int_{p_t}^{p_s} \sqrt{(uq)^2 + (vq)^2} \, dp \tag{2}$$

where ρ is water density (kg·m^{-3}), g is gravitational acceleration (m·s^{-2}), p_t is pressure at the top of the atmosphere (Pa), p_s is the near-surface pressure (Pa), q is specific humidity (kg·kg^{-1}), v is meridional wind (m·s^{-1}), and u is zonal wind (m·s^{-1}). As with PRCPTOT, VIWV and IWVT are normalized.

Pattern-based detection and attribution method
Different detection and attribution approaches[22,32,42,93,111–114] have been applied to extract the ACC signal from observed hydrological and meteorological variables. Here, we employ a pattern-based detection and attribution method[115–119] to capture the ACC signal in the observed increase in PRCPTOT over dry and wet regions. This method assumes the presence of characteristic patterns of climate response in different external forcings (fingerprints, which are a function of longitude and latitude). First, applying a rotated empirical orthogonal function (REOF)[45–47] decomposition to PRCPTOT CMIP6 simulations under H85 for dry and wet regions during 1901–2100, we obtain the spatial leading mode (EOF1; see Supplementary Fig. 10a–c for examples) from the spatio-temporal covariance matrix of PRCPTOT[43]. EOF1 is the fingerprint, which describes the response of PRCPTOT to external forcing in the historical period and in the future scenario of increasing greenhouse gas emissions.

We then project observed and simulated PRCPTOT $PRCP(i,j,t)$ onto the model-based fingerprints $F(i,j)$ (i.e. the EOF1) in dry and wet regions to quantify the ACC signal and noise arising from internal climate variability[43].

$$P(t) = \frac{\sum_{i\in lon_S, j\in lat_S} F(i,j)A(i,j)PRCP(i,j,t)}{\sum_{i\in lon_S, j\in lat_S} A(i,j)} \tag{3}$$

where $P(t)$ is the projection in year t, A is the gird area over region S (dry/wet regions), and i/j is the longitude/latitude of a grid cell in the dry/wet regions. If the fingerprint is becoming increasingly apparent in the PRCPTOT, there will exist an upward trend, which describes the spatial covariance between the PRCPTOT and the fingerprint as a function of time. In contrast, a negative trend indicates that the PRCPTOT and fingerprint are increasingly dissimilar. We calculate the L-length trend in $P(t)$ as the ACC signal $S(L)$[43,48], which is a single scalar signal of reduced dimensionality from the spatio-temporal PRCPTOT in the dry/wet regions. In this study, L is set to 58 (length of the period from 1961–2018).

To assess the significance of the ACC signal, we project the internal climate variability (PRCPTOT from the CMIP6 PiControl simulations) onto the fingerprint. For a signal of length L years, the noise $N(L)$ is represented as the standard deviation of all L-length trends in these projections under PiControl. Finally, we calculate the dimensionless signal-to-noise ratio: $SNR = S(L)/N(L)$, which provides a measure of the signal's significance (the likelihood of detecting an ACC signal relative to internal climate variability). If SNR exceeds 1.64 or 2.57, the forcing signal is considered detectable at the 90% or 99% confidence level[120]. SNR is also used to estimate time of emergence, which is the expected year from which the forcing signals start to emerge relative to natural climate variability.

Optimal fingerprinting method
In addition to the spatial fingerprint extracted by the REOF method, the optimal fingerprinting method[50,51,121] can detect the temporal fingerprint by regressing the observed changes ($\mathbf{Y}$) against the model simulated changes ($\mathbf{X}$)[93,122]. Specifically, the observed changes are assumed as the linear sum of

responses to external forcings, plus internal climate variability. The single-signal analyses are computed as follows:

$$\mathbf{Y} = (\mathbf{X} - \alpha)\beta + \varepsilon \tag{4}$$

where $\mathbf{Y}$ is the observed PRCPTOT, $\mathbf{X}$ is the simulated PRCPTOT under individual external forcing, α is the sampling uncertainty of $\mathbf{X}$, β is the scaling factor that scales $\mathbf{X}$ to match the long-term changes of $\mathbf{Y}$, and ε is the climate internal variability estimated from PiControl simulations. We also use two-signal analyses to separate contributions from NAT and other external forcings (e.g., GHG and AER) to observed trends[9]:

$$\mathbf{Y} = (\mathbf{X_{NAT}} - \alpha_{NAT})\beta_{NAT} + (\mathbf{X_{other}} - \alpha_{other})\beta_{other} + \varepsilon \tag{5}$$

where the subscript *other* indicates the external forcing excluding NAT (e.g., ALL, ANT, GHG, and AER). The regression is resolved by using ordinary least squares (OLS) and total least squares (TLS)[51], respectively. To reduce noise from interannual variability[91], the area-averaged time series of PRCPTOT in dry and wet regions are averaged over consecutive 3 year intervals. The β values provide a measure of the (un)certainty with whether a particular external forcing is detected. If the 90% confidence interval (CI) of β is above zero, the corresponding external signal is detectable at a significance level of 5%. The attributable PRCPTOT trends in dry and wet regions are quantified by multiplying the β with the linear trends of the simulations under different external forcings. The attributable PRCPTOT trends and their uncertainties are then compared with the observed PRCPTOT trend to estimate the contributions of different external forcing signals to PRCPTOT in dry and wet regions[35,110].

Data availability
All datasets used in this study are available online. The HadEx3 dataset is available at https://www.metoffice.gov.uk/hadobs/hadex3/; the CRU dataset is available at http://crudata.uea.ac.uk/cru/data/hrg/cru_ts_4.05/; the GPCC dataset is available at https://opendata.dwd.de/climate_environment/GPCC/html/download_gate.html; the GLEAM dataset is available at https://www.gleam.eu/; the CMIP6 model simulations are available at https://esgf-node.llnl.gov/search/cmip6/.

Code availability
The R (version 4.1.2) codes used in this study are available from the corresponding author (X.G.) upon reasonable request.

References
1. Wu, P., Christidis, N. & Stott, P. Anthropogenic impact on earth's hydrological cycle. *Nat. Clim. Change* **3**, 807–810 (2013).
2. Bullock, A. & Acreman, M. The role of wetlands in the hydrological cycle. *Hydrol. Earth Syst. Sci.* **7**, 358–389 (2003).
3. Wang, F. et al. Comprehensive evaluation of hydrological drought and its relationships with meteorological drought in the Yellow River basin, China. *J. Hydrol.* **584**, 124751 (2020).
4. Zhang, Q. et al. Divergent effectiveness of irrigation in enhancing food security in droughts under future climates with various emission scenarios. *Npj. Clim. Atmos. Sci.* **6**, 40 (2023).
5. Gampe, D. et al. Increasing impact of warm droughts on northern ecosystem productivity over recent decades. *Nat. Clim. Change* **11**, 772–779 (2021).
6. Wu, P., Wood, R., Ridley, J. & Lowe, J. Temporary acceleration of the hydrological cycle in response to a CO_2 rampdown. *Geophys. Res. Lett.* **37**, L12705 (2010).
7. Held, I. M. & Soden, B. J. Robust responses of the hydrological cycle to global warming. *J. Clim.* **19**, 5686–5699 (2006).
8. Roderick, M. L., Sun, F., Lim, W. H. & Farquhar, G. D. A general framework for understanding the response of the water cycle to global warming over land and ocean. *Hydrol. Earth Syst. Sci.* **18**, 1575–1589 (2014).
9. Zhang, X. et al. Detection of human influence on twentieth-century precipitation trends. *Nature* **448**, 461–465 (2007).
10. Emori, S. & Brown, S. J. Dynamic and thermodynamic changes in mean and extreme precipitation under changed climate. *Geophys. Res. Lett.* **32**, L17706 (2005).
11. Chou, C. & Lan, C.-W. Changes in the annual range of precipitation under global warming. *J. Clim.* **25**, 222–235 (2012).
12. Donat, M. G. et al. Updated analyses of temperature and precipitation extreme indices since the beginning of the twentieth century: The HadEX2 dataset. *J. Geophys. Res. Atmos.* **118**, 2098–2118 (2013).
13. Chadwick, R., Boutle, I. & Martin, G. Spatial patterns of precipitation change in CMIP5: why the rich do not gt richer in the tropics. *J. Clim.* **26**, 3803–3822 (2013).
14. Donat, M. G., Lowry, A. L., Alexander, L. V., O'Gorman, P. A. & Maher, N. More extreme precipitation in the world's dry and wet regions. *Nat. Clim. Change* **6**, 508–513 (2016).
15. Greve, P. et al. Global assessment of trends in wetting and drying over land. *Nat. Geosci.* **7**, 716–721 (2014).
16. Fowler, H. J. et al. Anthropogenic intensification of short-duration rainfall extremes. *Nat. Rev. Earth Environ.* **2**, 107–122 (2021).
17. Zhang, W. et al. Increasing precipitation variability on daily-to-multiyear time scales in a warmer world. *Sci. Adv.* **7**, eabf8021 (2021).
18. Seager, R., Naik, N. & Vecchi, G. A. Thermodynamic and dynamic mechanisms for large-scale changes in the hydrological cycle in response to global warming*. *J. Clim.* **23**, 4651–4668 (2010).
19. Huang, Z., Tan, X., Gan, T. Y., Liu, B. & Chen, X. Thermodynamically enhanced precipitation extremes due to counterbalancing influences of anthropogenic greenhouse gases and aerosols. *Nat. Water* **1**, 614–625 (2023).
20. Zaitchik, B. F., Rodell, M., Biasutti, M. & Seneviratne, S. I. Wetting and drying trends under climate change. *Nat. Water* **1**, 502–513 (2023).
21. Chadwick, R., Ackerley, D., Ogura, T. & Dommenget, D. Separating the influences of land warming, the direct CO_2 effect, the plant physiological effect, and SST warming on regional precipitation changes. *J. Geophys. Res. Atmos.* **124**, 624–640 (2019).
22. Tan, X. et al. Increasing global precipitation whiplash due to anthropogenic greenhouse gas emissions. *Nat. Commun.* **14**, 2796 (2023).
23. Persad, G. G. & Caldeira, K. Divergent global-scale temperature effects from identical aerosols emitted in different regions. *Nat. Commun.* **9**, 3289 (2018).
24. Haywood, J. M. et al. The roles of aerosol, water vapor and cloud in future global dimming/brightening. *J. Geophys. Res.* **116**, D20203 (2011).
25. Lin, L., Wang, Z., Xu, Y., Fu, Q. & Dong, W. Larger sensitivity of precipitation extremes to aerosol than greenhouse gas forcing in CMIP5 models. *J. Geophys. Res. Atmos.* **123**, 8062–8073 (2018).
26. Peng, D., Zhou, T., Zhang, L. & Wu, B. Human contribution to the increasing summer precipitation in central Asia from 1961 to 2013. *J. Clim.* **31**, 8005–8021 (2018).
27. Zhou, T. et al. The dynamic and thermodynamic processes dominating the reduction of global land monsoon precipitation driven by anthropogenic aerosols emission. *Sci. China Earth Sci.* **63**, 919–933 (2020).
28. Polson, D., Hegerl, G. C., Zhang, X. & Osborn, T. J. Causes of robust seasonal land precipitation changes*. *J. Clim.* **26**, 6679–6697 (2013).
29. Wan, H., Zhang, X., Zwiers, F. & Min, S.-K. Attributing northern high-latitude precipitation change over the period 1966–2005 to human influence. *Clim. Dyn.* **45**, 1713–1726 (2015).

30. Eyring, V. et al. Overview of the coupled model intercomparison project phase 6 (CMIP6) experimental design and organization. *Geosci. Model Dev.* **9**, 1937–1958 (2016).

31. Paik, S. et al. Determining the anthropogenic greenhouse gas contribution to the observed intensification of extreme precipitation. *Geophys. Res. Lett.* **47**, e2019GL086875 (2020).

32. Dai, A. Increasing drought under global warming in observations and models. *Nat. Clim. Change* **3**, 52–58 (2013).

33. Huang, J., Yu, H., Guan, X., Wang, G. & Guo, R. Accelerated dryland expansion under climate change. *Nat. Clim. Change* **6**, 166–171 (2016).

34. Feng, S. & Fu, Q. Expansion of global drylands under a warming climate. *Atmos. Chem. Phys.* **13**, 10081–10094 (2013).

35. Feng, S. et al. Greenhouse gas emissions drive global dryland expansion but not spatial patterns of change in aridification. *J. Clim.* **35**, 2901–2917 (2022).

36. Donat, M. G., Angélil, O. & Ukkola, A. M. Intensification of precipitation extremes in the world's humid and water-limited regions. *Environ. Res. Lett.* **14**, 065003 (2019).

37. Li, X., Ting, M. & Lee, D. E. Fast adjustments of the Asian summer monsoon to anthropogenic aerosols. *Geophys. Res. Lett.* **45**, 1001–1010 (2018).

38. Li, Z. et al. Aerosol and monsoon climate interactions over Asia. *Rev. Geophys.* **54**, 866–929 (2016).

39. Swart, N. C. et al. The canadian earth system model version 5 (CanESM5.0.3). *Geosci. Model Dev.* **12**, 4823–4873 (2019).

40. Liang, J., Liu, X., AghaKouchak, A., Ciais, P. & Fu, B. Asymmetrical precipitation sensitivity to temperature across global dry and wet regions. *Earths Future* **11**, e2023EF003617 (2023).

41. Sarojini, B. B., Stott, P. A. & Black, E. Detection and attribution of human influence on regional precipitation. *Nat. Clim. Change* **6**, 669–675 (2016).

42. Marvel, K. & Bonfils, C. Identifying external influences on global precipitation. *Proc. Natl Acad. Sci. USA* **110**, 19301–19306 (2013).

43. Marvel, K. et al. Twentieth-century hydroclimate changes consistent with human influence. *Nature* **569**, 59–65 (2019).

44. Bonfils, C. J. W. et al. Human influence on joint changes in temperature, rainfall and continental aridity. *Nat. Clim. Change* **10**, 726–731 (2020).

45. Mestas-Nunez, A. M. Orthogonality properties of rotated empirical modes. *Int. J. Climatol.* **20**, 1509–1516 (2000).

46. Greenacre, M. et al. Principal component analysis. *Nat. Rev. Methods Prim.* **2**, 100 (2022).

47. Hannachi, A., Jolliffe, I. T. & Stephenson, D. B. Empirical orthogonal functions and related techniques in atmospheric science: A review. *Int. J. Climatol.* **27**, 1119–1152 (2007).

48. Santer, B. D. et al. Separating signal and noise in atmospheric temperature changes: the importance of timescale. *J. Geophys. Res. Atmos.* **116**, 105 (2011).

49. Santer, B. D. et al. Identifying human influences on atmospheric temperature. *Proc. Natl Acad. Sci. USA* **110**, 26–33 (2013).

50. Allen, M. R. & Tett, S. F. B. Checking for model consistency in optimal fingerprinting. *Clim. Dyn.* **15**, 419–434 (1999).

51. Allen, M. R. & Stott, P. A. Estimating signal amplitudes in optimal fingerprinting, part I: theory. *Clim. Dyn.* **21**, 477–491 (2003).

52. Peng, D. & Zhou, T. Why was the arid and semiarid northwest China getting wetter in the recent decades. *J. Geophys. Res. Atmos.* **122**, 9060–9075 (2017).

53. Gimeno, L. et al. Oceanic and terrestrial sources of continental precipitation. *Rev. Geophys.* **50**, RG4003 (2012).

54. Zahn, M. & Allan, R. P. Quantifying present and projected future atmospheric moisture transports onto land: landward atmospheric moisture transports. *Water Resour. Res.* **49**, 7266–7277 (2013).

55. Wang, C., Li, J., Zhang, F. & Yang, K. Changes in the moisture contribution over global arid regions. *Clim. Dyn.* **61**, 543–557 (2023).

56. Hu, P., Feng, G., Dogar, M. M., Cheng, J. & Gong, Z. Joint effect of East Asia-Pacific and Eurasian teleconnections on the summer precipitation in North Asia. *J. Meteorol. Res.* **34**, 559–574 (2020).

57. He, X. & Guan, H. Multiresolution analysis of precipitation teleconnections with large-scale climate signals: a case study in south Australia: multiresolution analysis of precipitation teleconnections. *Water Resour. Res.* **49**, 6995–7008 (2013).

58. Shen, Z. et al. Drying in the low-latitude Atlantic Ocean contributed to terrestrial water storage depletion across Eurasia. *Nat. Commun.* **13**, 1849 (2022).

59. Findell, K. L. et al. Rising temperatures increase importance of oceanic evaporation as a source for continental precipitation. *J. Clim.* **32**, 7713–7726 (2019).

60. He, J. & Soden, B. J. A re-examination of the projected subtropical precipitation decline. *Nat. Clim. Change* **7**, 53–57 (2017).

61. Zhou, S. et al. Soil moisture–atmosphere feedbacks mitigate declining water availability in drylands. *Nat. Clim. Change* **11**, 38–44 (2021).

62. Barnes, E. A. & Polvani, L. Response of the midlatitude jets, and of their variability, to increased greenhouse gases in the CMIP5 models. *J. Clim.* **26**, 7117–7135 (2013).

63. Yin, J. H. A consistent poleward shift of the storm tracks in simulations of 21st century climate. *Geophys. Res. Lett.* **32**, L18701 (2005).

64. Berg, A., Lintner, B., Findell, K. & Giannini, A. Soil moisture influence on seasonality and large-scale circulation in simulations of the west African monsoon. *J. Clim.* **30**, 2295–2317 (2017).

65. Wang, T. et al. Anthropogenic agent implicated as a prime driver of shift in precipitation in eastern China in the late 1970s. *Atmos. Chem. Phys.* **13**, 12433–12450 (2013).

66. Wei, W. et al. Spatiotemporal variability in extreme precipitation and associated large-scale climate mechanisms in central asia from 1950 to 2019. *J. Hydrol.* **620**, 129417 (2023).

67. Qing, Y., Wang, S., Yang, Z.-L. & Gentine, P. Soil moisture −atmosphere feedbacks have triggered the shifts from drought to pluvial conditions since 1980. *Commun. Earth Environ.* **4**, 254 (2023).

68. Guan, Y. et al. Spatio-temporal variations in global surface soil moisture based on multiple datasets: intercomparison and climate drivers. *J. Hydrol.* **625**, 130095 (2023).

69. Roderick, T. P., Wasko, C. & Sharma, A. Atmospheric moisture measurements explain increases in tropical rainfall extremes. *Geophys. Res. Lett.* **46**, 1375–1382 (2019).

70. Berg, A. et al. Land–atmosphere feedbacks amplify aridity increase over land under global warming. *Nat. Clim. Change* **6**, 869–874 (2016).

71. Chen, Z. et al. Global land monsoon precipitation changes in CMIP6 projections. *Geophys. Res. Lett.* **47**, e2019GL086902 (2020).

72. Endo, H. & Kitoh, A. Thermodynamic and dynamic effects on regional monsoon rainfall changes in a warmer climate. *Geophys. Res. Lett.* **41**, 1704–1711 (2014).

73. Hsu, P. et al. Increase of global monsoon area and precipitation under global warming: a robust signal. *Geophys. Res. Lett.* **39**, 2012GL051037 (2012).

74. Zhou, S., Huang, G. & Huang, P. Changes in the East Asian summer monsoon rainfall under global warming: moisture budget decompositions and the sources of uncertainty. *Clim. Dyn.* **51**, 1363–1373 (2018).

75. Webster, P. J. et al. Monsoons: processes, predictability, and the prospects for prediction. *J. Geophys. Res. Oceans* **103**, 14451–14510 (1998).

76. Tokinaga, H., Xie, S.-P., Deser, C., Kosaka, Y. & Okumura, Y. M. Slowdown of the walker circulation driven by tropical Indo-Pacific warming. *Nature* **491**, 439–443 (2012).

77. He, J. & Soden, B. J. Anthropogenic weakening of the tropical circulation: the relative roles of direct CO2 forcing and sea surface temperature change. *J. Clim.* **28**, 8728–8742 (2015).

78. Vecchi, G. A. et al. Weakening of tropical Pacific atmospheric circulation due to anthropogenic forcing. *Nature* **441**, 73–76 (2006).

79. Vecchi, G. A. & Soden, B. J. Global warming and the weakening of the tropical circulation. *J. Clim.* **20**, 4316–4340 (2007).

80. Lu, J., Vecchi, G. A. & Reichler, T. Expansion of the Hadley cell under global warming. *Geophys. Res. Lett.* **34**, L06805 (2007).

81. Kang, S. M. & Lu, J. Expansion of the Hadley cell under global warming: winter versus summer. *J. Clim.* **25**, 8387–8393 (2012).

82. Lau, W. K. M. & Kim, K.-M. Robust Hadley circulation changes and increasing global dryness due to CO_2 warming from CMIP5 model projections. *Proc. Natl Acad. Sci.* **112**, 3630–3635 (2015).

83. Karnauskas, K. B. & Ummenhofer, C. C. On the dynamics of the Hadley circulation and subtropical drying. *Clim. Dyn.* **42**, 2259–2269 (2014).

84. Liu, F. et al. Increased Asian aerosols drive a slowdown of Atlantic meridional overturning circulation. *Nat. Commun.* **15**, 18 (2024).

85. Rotstayn, L. D. et al. Declining aerosols in CMIP5 projections: effects on atmospheric temperature structure and midlatitude jets. *J. Clim.* **27**, 6960–6977 (2014).

86. Xie, X. et al. Anthropogenic sulfate aerosol pollution in south and east Asia induces increased summer precipitation over arid central asia. *Commun. Earth Environ.* **3**, 328 (2022).

87. Abbott, B. W. et al. Human domination of the global water cycle absent from depictions and perceptions. *Nat. Geosci.* **12**, 533–540 (2019).

88. Zhang, Y. et al. Coupled estimation of 500 m and 8-day resolution global evapotranspiration and gross primary production in 2002–2017. *Remote Sens. Environ.* **222**, 165–182 (2019).

89. Yang, Y. et al. Evapotranspiration on a greening Earth. *Nat. Rev. Earth Environ.* **4**, 626–641 (2023).

90. Zhang, Y. et al. Southern hemisphere dominates recent decline in global water availability. *Science* **382**, 579–584 (2023).

91. Liu, J. et al. Contributions of anthropogenic forcings to evapotranspiration changes over 1980–2020 using GLEAM and CMIP6 simulations. *J. Geophys. Res. Atmospheres* **126**, e2021JD035367 (2021).

92. Fyfe, J. C. et al. Large near-term projected snowpack loss over the western United States. *Nat. Commun.* **8**, 14996 (2017).

93. Gu, X. et al. Attribution of global soil moisture drying to human activities: a quantitative viewpoint. *Geophys. Res. Lett.* **46**, 2573–2582 (2019).

94. Gudmundsson, L., Seneviratne, S. I. & Zhang, X. Anthropogenic climate change detected in European renewable freshwater resources. *Nat. Clim. Change* **7**, 813–816 (2017).

95. McDermid, S. et al. Irrigation in the earth system. *Nat. Rev. Earth Environ.* **4**, 435–453 (2023).

96. Ni, J. et al. Three gorges dam: friend or foe of riverine greenhouse gases. *Natl Sci. Rev.* **9**, nwac013 (2022).

97. Kåresdotter, E., Destouni, G., Ghajarnia, N., Lammers, R. B. & Kalantari, Z. Distinguishing direct human-driven effects on the global terrestrial water cycle. *Earths Future* **10**, e2022EF002848 (2022).

98. Allen, M. R. & Ingram, W. J. Constraints on future changes in climate and the hydrologic cycle. *Nature* **419**, 228–232 (2002).

99. Liu, J. et al. Global changes in floods and their drivers. *J. Hydrol.* **614**, 128553 (2022).

100. Fu, J. et al. Extreme rainfall reduces one-twelfth of China's rice yield over the last two decades. *Nat. Food* **4**, 416–426 (2023).

101. Li, H. et al. Land–atmosphere feedbacks contribute to crop failure in global rainfed breadbaskets. *Npj Clim. Atmos. Sci.* **6**, 51 (2023).

102. Zhang, Y., Keenan, T. F. & Zhou, S. Exacerbated drought impacts on global ecosystems due to structural overshoot. *Nat. Ecol. Evol.* **5**, 1490–1498 (2021).

103. Yin, J. et al. Flash floods: why are more of them devastating the world's driest regions. *Nature* **615**, 212–215 (2023).

104. Dunn, R. J. H. et al. Development of an updated global land in situ-based data set of temperature and precipitation extremes: hadEX3. *J. Geophys. Res. Atmos.* **125**, e2019JD032263 (2020).

105. Harris, I., Osborn, T. J., Jones, P. & Lister, D. Version 4 of the CRU TS monthly high-resolution gridded multivariate climate dataset. *Sci. Data* **7**, 109 (2020).

106. Schneider, U., Hänsel, S., Finger, P., Rustemeier, E. & Ziese, M. GPCC full data monthly product version 2022 at 0.25°: monthly land-Surface precipitation from rain-gauges built on GTS-based and historical data. *DWD* https://doi.org/10.5676/DWD_GPCC/FD_M_V2022_050 (2022).

107. Sun, Q. et al. A Review of global precipitation data sets: data sources, estimation and intercomparisons. *Rev. Geophys.* **56**, 79–107 (2018).

108. Martens, B. et al. GLEAM v3: satellite-based land evaporation and root-zone soil moisture. *Geosci. Model Dev.* **10**, 1903–1925 (2017).

109. Peng, S., Ding, Y., Liu, W. & Li, Z. 1 km monthly temperature and precipitation dataset for China from 1901 to 2017. *Earth Syst. Sci. Data* **11**, 1931–1946 (2019).

110. Yuan, X. et al. A global transition to flash droughts under climate change. *Science* **380**, 187–191 (2023).

111. Hegerl, G. C. et al. Challenges in quantifying changes in the global water cycle. *Bull. Am. Meteorol. Soc.* **96**, 1097–1115 (2015).

112. StotT, P. A. et al. Future challenges in event attribution methodologies. *Bull. Am. Meteorol. Soc.* **99**, S155–S157 (2018).

113. Sippel, S., Meinshausen, N., Fischer, E. M., Székely, E. & Knutti, R. Climate change now detectable from any single day of weather at global scale. *Nat. Clim. Change* **10**, 35–41 (2020).

114. Duan, W. et al. Changes in temporal inequality of precipitation extremes over China due to anthropogenic forcings. *Npj Clim. Atmos. Sci.* **5**, 33 (2022).

115. Bonfils, C. et al. Detection and attribution of temperature changes in the mountainous western United States. *J. Clim.* **21**, 6404–6424 (2008).

116. Pierce, D. W. et al. Attribution of declining western U.S. snowpack to human effects. *J. Clim.* **21**, 6425–6444 (2008).

117. Barnett, T. P. et al. Human-induced changes in the hydrology of the western United States. *Science* **319**, 1080–1083 (2008).

118. Santer, B. D. et al. Human and natural influences on the changing thermal structure of the atmosphere. *Proc. Natl Acad. Sci. USA* **110**, 17235–17240 (2013).

119. Santer, B. D. et al. Identification of human-induced changes in atmospheric moisture content. *Proc. Natl Acad. Sci.* **104**, 15248–15253 (2007).

120. Mastrandrea, M. D. et al. *Guidance Note for Lead Authors of the IPCC Fifth Assessment Report on Consistent Treatment of Uncertainties* (IPCC, 2010).

121. Hegerl, G. C. et al. Detecting greenhouse-gas-induced climate change with an optimal fingerprint method. *J. Clim.* **9**, 2281–2306 (1996).

122. Kong, D., Gu, X., Li, J., Ren, G. & Liu, J. Contributions of global warming and urbanization to the intensification of human-perceived heatwaves 0ver China. *J. Geophys. Res. Atmospheres* **125**, e2019JD032175 (2020).

Acknowledgements

Author contributions

X.G. and X.Z. designed this study. Y.G. conducted the calculations and analyses. X.G. and Y.G. wrote the first draft. All the authors contributed to the discussion, editing, and improving the paper.

Competing interests

The authors declare no competing interests.

Additional information

Supplementary information The online version contains supplementary material available at https://doi.org/10.1038/s41612-024-00590-9.

Correspondence and requests for materials should be addressed to Xihui Gu or Xiang Zhang.

Reprints and permissions information is available at http://www.nature.com/reprints

Publisher's note Springer Nature remains neutral with regard to jurisdictional claims in published maps and institutional affiliations.

[1]Department of Atmospheric Science, School of Environmental Studies, China University of Geosciences, Wuhan 430074, China. [2]Key Laboratory of Meteorological Disaster Ministry of Education & Collaborative Innovation Center on Forecast and Evaluation of Meteorological Disasters, Nanjing University of Information Science & Technology, Nanjing 210044, China. [3]Institute of Arid Meteorology, China Meteorological Administration, Lanzhou 730020, China. [4]Key Lab of Basin Water Resource and Eco-environmental Science in Hubei Province, Wuhan 430010, China. [5]The National Key Laboratory of Water Disaster Prevention, Nanjing Hydraulic Research Institute, Nanjing 210029, China. [6]Hubei Key Laboratory of Yangtze Catchment Environmental Aquatic Science, Wuhan 430074, China. [7]Centre for Severe Weather and Climate and Hydro-geological Hazards, Wuhan 430074, China. [8]School of Geography and the Environment, University of Oxford, Oxford, UK. [9]Department of Remote Sensing, Helmholtz Centre for Environmental Research – UFZ, 04318 Leipzig, Germany. [10]Department of Geography and Resource Management, The Chinese University of Hong Kong, Hong Kong, China. [11]Hubei Key Laboratory of Regional Ecology and Environmental Change, School of Geography and Information Engineering, China University of Geosciences, Wuhan 430074, China. [12]State Key Laboratory of Biogeology and Environmental Geology, China University of Geosciences, Wuhan 430074, China. [13]Guangdong-Hong Kong Joint Laboratory for Water Security, Beijing Normal University at Zhuhai, Zhuhai 519087, China. [14]Water Security Research Institute, Beijing Normal University at Zhuhai, Zhuhai 519087, China. [15]National Engineering Research Center of Geographic Information System, School of Geography and Information Engineering, China University of Geosciences, Wuhan 430074, China. ✉e-mail: guxh@cug.edu.cn; zhangxiang76@cug.edu.cn